Acta Oceanol. Sin., 2021, Vol. 40, No. 3, P. 112–121
https://doi.org/10.1007/s13131-021-1715-4
http://www.hyxb.org.cn
E-mail: hyxbe@263.net

Ocean surface current retrieval and imaging with a new shore-based X-band radar based on time-shifted up-and-down linear frequency modulated signal

Yijun He[1, 2], Xin Song[1], Baochang Liu[1]*, Na Yi[1], Xiuzhong Li[1]

[1] School of Marine Sciences, Nanjing University of Information Science and Technology, Nanjing 210044, China

[2] Laboratory for Regional Oceanography and Numerical Modeling, Pilot National Laboratory for Marine Science and Technology (Qingdao), Qingdao 266237, China

Received 22 April 2020; accepted 18 May 2020

Abstract

This paper proposes a multifunction radar that can not only measure sea currents but also perform sea-surface imaging. The fundamental aspect of the proposed radar comprises transmitting time-shifted up-and-down continuous wave linear frequency modulated signals that allow for the offset of two one-dimensional range images of the sea surface that respectively correspond to the upward linear frequency modulated (LFM) signal and the downward LFM signal. Owing to the Doppler frequency shift from the sea surface, a range offset, which is proportional to the radial velocity of the sea surface, occurs between the upward and downward LFM signals. By using the least-squares linear fitting method in the transformed domain, the range offset can be measured and the current velocity can be retrieved. Finally, we verify the accuracy of current measurement with simulation results.

Key words: shore-based radars, signal processing, ocean surface currents, up-and-down CWLFM

Citation: He Yijun, Song Xin, Liu Baochang, Yi Na, Li Xiuzhong. 2021. Ocean surface current retrieval and imaging with a new shore-based X-band radar based on time-shifted up-and-down linear frequency modulated signal. Acta Oceanologica Sinica, 40(3): 112–121, doi: 10.1007/s13131-021-1715-4

1 Introduction

The ocean is the largest water body on earth, covering about three-quarters of its surface. It is a global climate regulator and a treasure trove of resources for the world. Ocean current is the directional current of seawater. The real-time monitoring of current is of great significance for marine ecology, maritime transportation, marine development, and the military. When the current carries heat from a low latitude to a high latitude, it increases water vapor transport and produces precipitation. For the military, currents have a significant influence on underwater vehicle navigation (Zhang et al., 2016). Therefore, the observation of currents is very important.

Existing current measurement methods include satellites, shore-based radars, and *in situ* current measurement. Satellite remote sensing images are expensive, have low repetitive sampling times, and are susceptible to severe ocean weather (Bao et al., 2015). Although *in situ* current measurement has high observation accuracy, its spatial coverage is limited. It is difficult to use it to investigate the temporal and spatial changes in ocean currents, and the observation cost is high (Klemas, 2012). Shore-based radars can continuously measure current field in coastal waters in real-time, thus compensating for these shortcomings.

There are two main types of shore-based radars: high-frequency (HF) radar and X-band radar. HF radar can measure sea surface currents, waves and wind parameters (Maresca et al., 2014). HF radar emits electromagnetic waves to the sea surface, and the surface velocity of the ocean is measured by the received backscattered Doppler spectrum (Barrick, 1972). A single-station radar can only measure the surface current velocity in the radial direction. Therefore, it is necessary to use two different positions of the radar to generate the current vector field. X-band radar can image both the spatial and temporal variations of the sea surface with high resolutions (Huang et al., 2017a). This radar emits electromagnetic waves to the surface of the sea, and by analyzing the received backscattering information, it is possible to obtain information on the surface current (Wang et al., 2007; Senet et al., 2008). It also has been used in the monitoring of nearshore environments, such as waves (Young et al., 1985), bathymetry, and wind (Lund et al., 2012). Furthermore, X-band marine radar is widely installed on ships for navigation purposes, which can significantly reduce the costs associated with traditional *in situ* sensors (Huang et al., 2017a). Although the aforementioned two radar types can measure the sea-surface current, they each have their shortcomings. Although the HF radar considers the Doppler information on the ocean current motion, there is no image near the radar due to interference. As the distance from the radar increases, the echo gradually weakens and the imaging gradually blurs. The X-band radar obtains ocean wave information through images and then obtains ocean current information (Gangeskar, 2018). But when we use it to calculate the sea surface current speed, it needs to remove the speed of the Bragg scattering waves and the wind-induced surface drift due to wind shear stress at the air-sea boundary layer (Carrasco et al., 2017; Seemann et al.,

Foundation item: The National Key Research and Development Program under contract No. 2016YFC1401002; the National Natural Science Foundation of China under contract Nos 41606201, 41576173, 41620104003 and 41706202.
*Corresponding author, E-mail: bcliu@nuist.edu.cn

2017; Al-Habashneh et al., 2018). These cannot be calculated accurately. The accuracy current measurement cannot be guaranteed. Therefore, it needs to develop a multifunction radar that can perform both current measurement and imaging. The purpose of this study is to develop an improved shore-based X-band radar that can simultaneously measure sea currents and image the ocean surface. To this end, we propose the use of time-shifted up-and-down continuous wave linear frequency modulated (CWLFM) signals as the radar-transmitted signals. Compared with the non-linear frequency modulated signal, linear frequency modulated signal has higher average power. Because of the Doppler frequency shift which results from the sea surface, a range offset, which is proportional to the radial velocity of the sea surface, occurs between the two one-dimensional (1-D) range images of the sea surface that respectively correspond to the upward and downward linear frequency modulated (LFM) signals. Using the least-squares linear fitting method in the transformed domain, the range offset can be measured and then the current velocity can be retrieved.

Up-and-down LFM signals were also applied to a spaceborne fixed-sector scatterometer by Fois et al. (2015) for current measurement. The main difference between our method and that in Fois et al. (2015) is that in their method, simultaneously-transmitted up-and-down signals are used, whereas, in our method, time-shifted LFM signals are adopted. When the radar simultaneously transmits the up-and-down LFM signals, the received original signal overlaps in both time and frequency domain. When we de-chirping, and performing the Fourier transform (FT) on the upward LFM signal, the downward LFM signal will be defocused. The defocus energy of the downward LFM signals is like noise in the upward LFM signal. This is what we call the interference. When a distributed scene that consists of a multitude of scatterers is considered, after de-chirping, and performing the Fourier transform (FT) on the upward LFM signal of each scatterer, the downward LFM signal of each scatterer will be defocused, and influence with each other. At this case, for the upward LFM signal of a certain scatterer, expect the defocus energy of this scatterer's downward LFM component, the defocus energy of the downward LFM signals of the other scatterers will also influence this scatterer. The energy from other scatterers accumulates like noise in the upward LFM signal, which obviously affects the accuracy of current measurement. In order to solve this problem, we propose, in this paper, to use time-shifted, rather than simultaneously-transmitted, up and down LFM signals. This method not only solves the problem of interference but also improves current measurement accuracy. In this paper, we also present the complete procedures of current retrieval for a distributed moving ocean surface, which were not provided in the work of Fois et al. (2015). What's more, Fois et al. (2015) only use a single point-like target to demonstrate the principle of their methods.

2 Velocity measurement principle

This section is intended to introduce the fundamental principle of velocity measurement based on up-and-down LFM signals. By using a point-like target, the velocity measuring principle of the method (Fois et al., 2015) that involves the simultaneous transmission of up-and-down LFM signals is first explained, followed by an explanation of a problem with this method encountered when a distributed ocean scene is considered. Then, we formulate a scheme that uses time-shifted, instead of simultaneously-transmitted, up-and-down LFM signals to solve the aforementioned problem.

2.1 *Velocity measurement principle based on up-and-down LFM signals*

We attempt to explain the principle of velocity measurement based on up-and-down CWLFM signals in a simple way by considering a single point-like target located within the footprint of the shore-based radar. As illustrated in Fig. 1, the x-axis represents time, the y-axis represents frequency, the dotted lines represent the frequency-versus-time signatures of the transmitted up-and-down CWLFM signals and the solid lines represent the received signals backscattered from the point target which are time-delayed copies of the transmitted signals. Upon multiplying the received signal with the complex conjugate of the transmitted signal, a process called de-chirping, and performing the Fourier transform (FT) on the resultant signal, we can obtain two sinc-function-shaped range-compressed 1-D images of the point target expressed in the frequency domain, with one corresponding to the upward LFM signal and the other to the downward LFM signal, as shown in the lower part of Fig. 1. When the point target velocity is zero, there will be no Doppler frequency shift. As

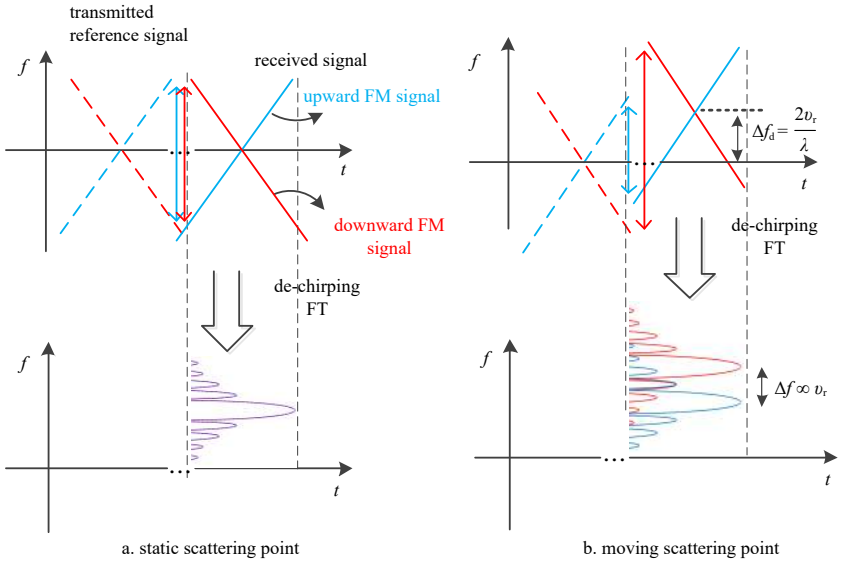

Fig. 1. A schematic diagram of up-and-down linear frequency modulated (LFM) signal speed measurement.

shown in Fig. 1a, the obtained upward and downward LFM signals completely overlap in the frequency domain. When the target velocity is not zero, the signal is shifted because of the Doppler effect. Because the upward LFM signal and the downward LFM signal will each produce a Doppler shift Δf_{d}, the two directions are opposite, the range offset between the upward LFM signal and the downward one is twice of Doppler shift. As indicated in Fig. 1b, when we de-chirp the received upward and downward LFM signals and apply a FT, there will be an offset Δf which is proportional to the target radial velocity v_{r}, which is expressed as

$$\Delta f = \frac{4v_{\mathrm{r}}}{\lambda} = 2\Delta f_{\mathrm{d}}, \tag{1}$$

where λ is the radar electromagnetic wave wavelength and Δf is the range offset. Hence, we can measure the velocity based on the offset of the received signal in the frequency domain.

When we consider a single scatterer, after de-chirping, and performing the FT on the upward echo, though the downward echo is defocused, however there is no defocus energy from other scatterers. At this case, the interference is relatively small, and has little effect on current measurement. When we consider a distributed scene that consists of a multitude of scatters, after de-chirping, and performing the FT on the upward LFM signal of each scatterer, the downward LFM signal of each scatterer will be defocused, and influence with each other. At this case, for the upward LFM signal of a certain scatterer, expect the defocus energy of this scatterer's downward LFM component, the defocus energy of the downward LFM signals of the other scatterers will also influence this scatterer. The energy from other scatterers accumulates like noise in the upward LFM signal. It obviously affects the current measuring accuracy. So, the simultaneously-transmitted signals pose little effect on velocity measurement when a single target is considered. But it obviously affects the current measuring accuracy when a distributed scene that consists of a multitude of scatterers is considered. Fois et al. (2015) considered only a scatterer when they measured the current field velocity using this principle. They did not consider measuring the current's velocity in a region, nor the problem of up-and-down LFM signals interfering with each other. Based on this, we propose a new signal transmission method that uses time-shifted up-and-down CWLFM signals.

2.2 *Velocity measurement principle based on time-shifted up-and-down CWLFM signals*

We consider a right-hand Cartesian coordinate system, as shown in Fig. 2, where the xy plane is locally tangent to the surface of the earth. In this coordinate system, an X-band shore-based radar works at the altitude of h. The shaded area in Fig. 2 is the radar's illuminated area. L_{r} is the range length of the radar's illuminated area. The red solid point (R_0, φ_0) is the reference point of the observation center.

To solve the problem of interference between the upward and downward LFM signals, we use the X-band shore-based radar to transmit the time-shifted up-and-down CWLFM signals, which can be written as

$$S_{\mathrm{tran}}(t) = \left[W_{\mathrm{r}}(t)\,\mathrm{e}^{j\pi k_{\mathrm{r}} t^2} + W_{\mathrm{r}}(t-\Delta t)\,\mathrm{e}^{-j\pi k_{\mathrm{r}}(t-\Delta t)^2}\right]\mathrm{e}^{j2\pi f_0 t}, \tag{2}$$

where k_{r} is the LFM rate of the transmitted pulse, the unit of k_{r} is Hz/s, t is the transmission time, j is the imaginary unit, and f_0 is the X-band radar carrier frequency. $W_{\mathrm{r}}(t)$ is the modulation envelope of the upward LFM signal, it is defined as

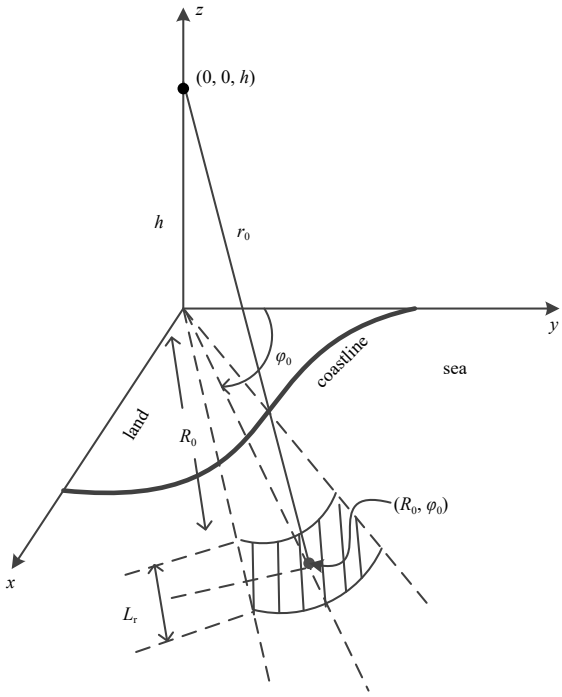

Fig. 2. The ocean scene's geometry. φ_0 is the radar observation azimuth, the shaded area is the radar range, and R_0 is the horizontal distance of the radar platform from the observation area.

$$W_{\mathrm{r}}(t) = \begin{cases} 1, & |t| \leqslant \dfrac{T_{\mathrm{r}}}{2} \\ 0, & \text{else} \end{cases}, \tag{3}$$

where T_{r} is the modulated duration of the upward and downward LFM signals. Furthermore, in Eq. (2), Δt denotes the interval between the upward and downward LFM signals, which is defined by

$$\Delta t = T_{\mathrm{r}} + \frac{2L_{\mathrm{r}}}{c}, \tag{4}$$

where c is the speed of light, and $2L_{\mathrm{r}}/c$ is the interval between the up-and-down LFM signals. The signals we transmitted are shown in Fig. 3. When we measure a distributed scene that consists of a multitude of scatterers, because the received signals backscattered from the point target are time-delayed copies of the transmitted signals, the upward and downward LFM radar echo of the respective target points are separated. As shown in Fig. 4, when the radar receives the radar echo, we can separate and de-chirp the upward LFM echo and downward LFM echo separately. Therefore, the problem of these signals interfering with each other can be solved. The velocity measurement principle based on time-shifted up-and-down LFM signals is consistent with the simultaneously-transmitted up-and-down LFM signals.

3 Processing steps

Based on the proposed velocity measurement principle, we retrieve the sea-surface current velocity in a region using time-shifted up-and-down CWLFM signals. This section describes the specific steps for measuring the current velocity by using time-shifted up-and-down CWLFM signals. In addition, we also provide specific steps for imaging the sea-surface. Figure 5 shows the specific steps for measuring the current velocity.

3.1 *Velocity retrieval*

3.1.1 *Down-converting and separating the sea-surface radar echo*

Down-conversion of the received sea-surface signal $S_{\mathrm{recv}}(t)$ to remove the carrier frequency is performed according to the following:

$$\tilde{S}_{\mathrm{recv}}(t) = S_{\mathrm{recv}}(t)\,\mathrm{e}^{-j2\pi f_0 t}. \tag{5}$$

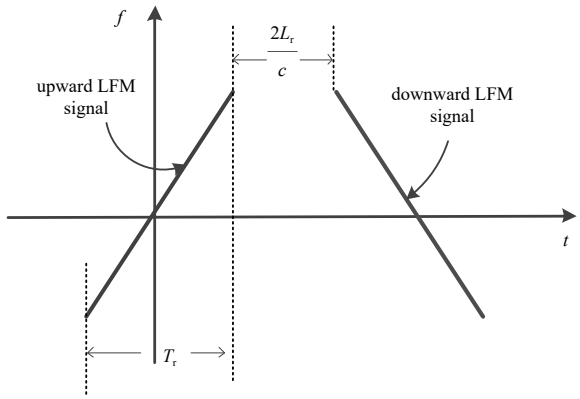

Fig. 3. A diagram of radar-transmitted signals. The ordinate f represents the frequency and the sweep slope is k_{r}.

Then, we can separate the upward and downward LFM signals, according to the following:

$$S_{\mathrm{recv}}^{\mathrm{up}}(t) = \tilde{S}_{\mathrm{recv}}\left(t + \frac{2r_0}{c}\right) \cdot \mathrm{rect}\left(\frac{t}{\Delta t}\right), \tag{6}$$

$$S_{\mathrm{recv}}^{\mathrm{dw}}(t) = \tilde{S}_{\mathrm{recv}}\left(t + \frac{2r_0}{c} + \Delta t\right) \cdot \mathrm{rect}\left(\frac{t}{\Delta t}\right), \tag{7}$$

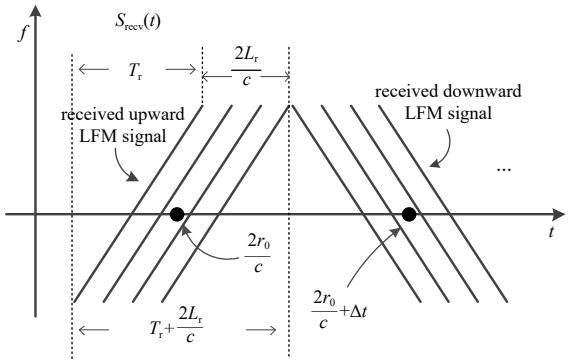

Fig. 4. A diagram of a received signal's time-frequency characteristics. The filled black circle in the figure is the scene's center reference point.

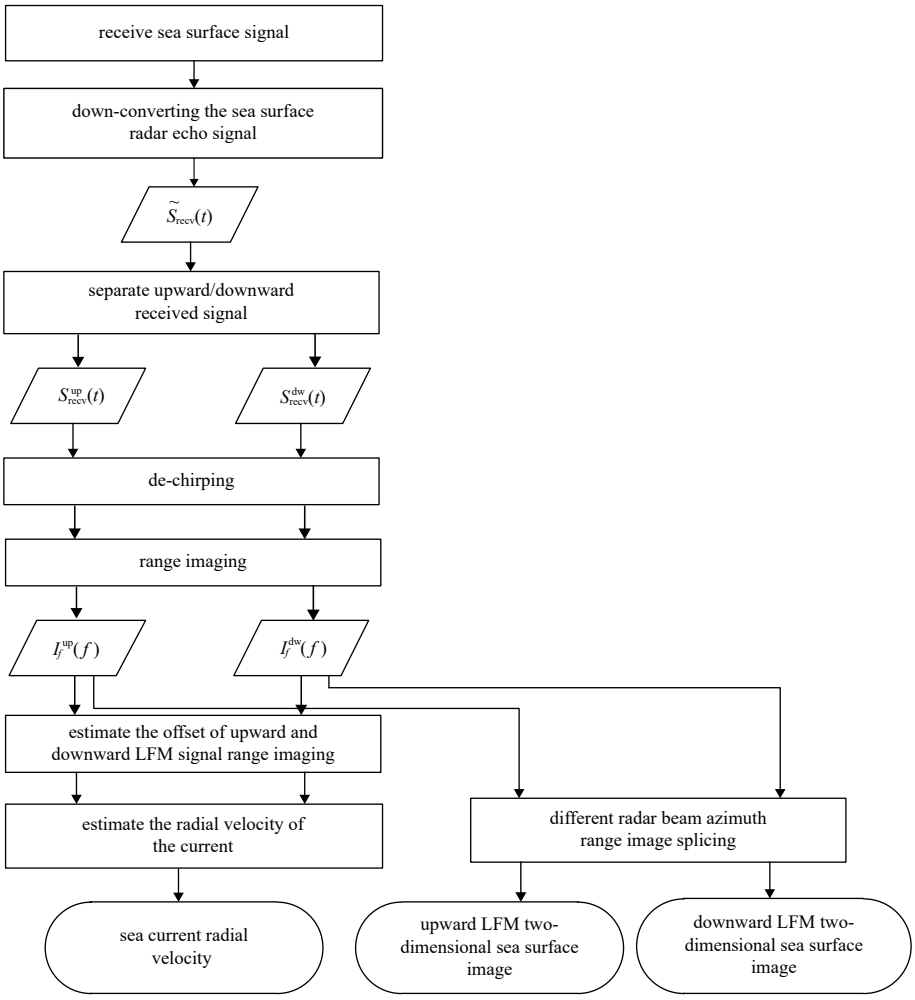

Fig. 5. The flow chart for retrieving sea-current speed.

where r_0 is the slant distance of the radar beam from the center of the illuminated area of the sea to the radar, as is shown in Fig. 2, and rect $\left(\frac{t}{\Delta t}\right)$ is a rectangular window function, given by

$$\text{rect}\left(\frac{t}{\Delta t}\right)=\begin{cases}1, & |t|\leqslant\frac{\Delta t}{2}\\ 0, & \text{else}\end{cases}. \tag{8}$$

3.1.2 *De-chirping the upward LFM signal and downward LFM signals*

To obtain 1-D range images of the sea surface that respectively correspond to the upward and downward LFM signals, we de-chirp the upward and downward LFM signals according to

$$S_{\text{decp}}^{\text{up}}(t)=S_{\text{recv}}^{\text{up}}(t)\left(S_{\text{ref}}^{\text{up}}(t)\right)^{*}, \tag{9}$$

$$S_{\text{decp}}^{\text{dw}}(t)=S_{\text{recv}}^{\text{dw}}(t)\left(S_{\text{ref}}^{\text{dw}}(t)\right)^{*}, \tag{10}$$

where $(\cdot)^{*}$ stands for a complex conjugate; $S_{\text{decp}}^{\text{up}}(t)$ and $S_{\text{decp}}^{\text{dw}}(t)$ represent the upward LFM signal and the downward LFM signal after de-chirping, respectively; $S_{\text{ref}}^{\text{up}}(t)$ and $S_{\text{ref}}^{\text{dw}}(t)$ represent the upward frequency reference signal and the downward frequency reference signal for de-chirping, respectively, which are expressed by

$$S_{\text{ref}}^{\text{up}}(t)=\text{rect}\left(\frac{t}{\Delta t}\right)\text{e}^{j\pi k_{\text{r}}t^{2}}, \tag{11}$$

$$S_{\text{ref}}^{\text{dw}}(t)=\text{rect}\left(\frac{t}{\Delta t}\right)\text{e}^{-j\pi k_{\text{r}}t^{2}}. \tag{12}$$

3.1.3 *Range imaging*

The pulse-compressed downward LFM signal is taken in a conjugate form. The FT and the modulo operator are used to perform range imaging on the upward and downward LFM signals according to the following:

$$I_{f}^{\text{up}}(f)=\left|\text{FT}\left\{S_{\text{decp}}^{\text{up}}(t)\right\}\right|, \tag{13}$$

$$I_{f}^{\text{dw}}(f)=\left|\text{FT}\left\{S_{\text{decp}}^{\text{dw}\ *}(t)\right\}\right|, \tag{14}$$

where FT $\{\cdot\}$ represents the Fourier transform operator, $I_{f}^{\text{up}}(f)$ and $I_{f}^{\text{dw}}(f)$ represent the upward frequency one-dimensional range image and the downward frequency one-dimensional range image in the frequency domain, respectively.

3.1.4 *Estimation of the offset of the upward LFM signal range image and the downward LFM signal range image*

First, in order to calculate the phase difference between $I_{f}^{\text{up}}(f)$ and $I_{f}^{\text{dw}}(f)$ in transform domain, we use the inverse Fourier transform according to the following:

$$I_{t}^{\text{up}}(t)=\text{IFT}\left\{I_{f}^{\text{up}}(f)\right\}, \tag{15}$$

$$I_{t}^{\text{dw}}(t)=\text{IFT}\left\{I_{f}^{\text{dw}}(f)\right\}, \tag{16}$$

where IFT $\{\cdot\}$ denotes the Fourier inverter operator.

Then, we calculate the phase difference between the two images $I_{t}^{\text{up}}(t)$ and $I_{t}^{\text{dw}}(t)$ according to the following:

$$\Delta\phi(t)=\angle\left\{I_{t}^{\text{up}}(t)\ \left(I_{t}^{\text{dw}}(t)\right)^{*}\right\}, \tag{17}$$

where $\angle\{\cdot\}$ denotes taking the phase of a complex number.

As the median filtering is not affected by outlier data, we then use median filtering to smooth the phase difference to reduce the error. According to the principle analysis, when there is no noise, the phase difference with time should be a straight line. Thus, we use linear fitting. By using the least-squares linear fitting method in the transformed domain, we linearly fit $\Delta\phi(t)$ in the interval $-T_{\text{r}}\leqslant t\leqslant T_{\text{r}}$ to obtain a straight line:

$$\Delta\tilde{\phi}(t)=a\cdot t+b,\qquad -T_{\text{r}}\leqslant t\leqslant T_{\text{r}}, \tag{18}$$

where a is the slope of the fitted line, and b is a constant term. Then, based on the slope of the fitted line, we can obtain the offset of two 1-D range images of the sea surface that correspond to the upward and downward LFM signals, shown as

$$\Delta f=\frac{a}{2\pi}. \tag{19}$$

Finally, as the range offset Δf is proportional to the radial velocity of the sea surface, we can measure the sea surface current velocity via the following equation:

$$\widetilde{V}_{\text{r}}=\frac{\Delta f\cdot c}{4f_0+2\Delta t\cdot k_{\text{r}}}\approx\frac{\Delta f\cdot c}{4f_0}. \tag{20}$$

In Eq. (20), the Doppler shifted caused by the target is extracted through the diversity in the LFM signal. Then the speed is calculated. As shown in Fig. 5, after we obtain the two 1-D range images of the sea surface, we can also obtain the two-dimensional (2-D) range image of the sea surface. In the following section, we will provide specific experimental steps.

3.2 *Sea-surface imaging*

The proposed radar system is a composite function radar. It not only has a velocity measurement function but also has an imaging function that is different from that of the traditional shore-based radars. Given that the shore-based radar we designed is a rotary scanning radar, we use imaging splicing.

As shown in Fig. 6, first, when the X-band radar observes at the azimuth angle φ_0, we receive the radar echo of this launch. We use a two-scale model (Wright, 1968) to divide the sea surface into several scattering points. Then, we calculate the unit impulse response of a single scattering point based on the scattering principle, and sum all of the scattering points. Finally, we de-chirp the received signal and then image it. The one-dimensional range image $I_{f}^{\text{up}}(f)$, $I_{f}^{\text{dw}}(f)$ can be transformed from the frequency coordinate f to the slant range coordinate r according to

$$r=\frac{f}{k_{\text{r}}}\cdot\frac{c}{2}+\sqrt{h^{2}+R_{0}^{2}}, \tag{21}$$

where h is the height of the X-band shore-based radar, as is shown in Fig. 2.

After that, we can obtain the 1-D range images $I_{r}^{\text{up}}(r;\varphi_0)$ and

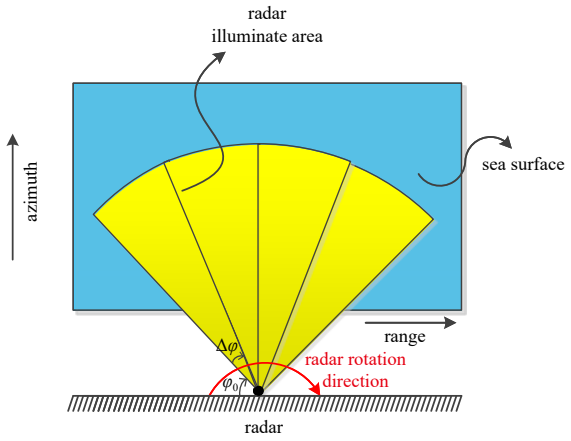

Fig. 6. Schematic of the radar's imaging function.

$I_r^{\mathrm{dw}}(r;\varphi_0)$ that correspond to the upward LFM signal and the downward LFM signal, respectively, at the slant range coordinates, with the parameter φ_0 denoting the azimuthal angle of radar observation as shown in Fig. 2.

Then, we transform the upward LFM signal and downward LFM signal 1-D range images $I_r^{\mathrm{up}}(r;\varphi_0)$ and $I_r^{\mathrm{dw}}(r;\varphi_0)$ from the slant range coordinate r to the ground distance coordinate R according to

$$R=\sqrt{r^2-h^2}, \tag{22}$$

to obtain $I_R^{\mathrm{up}}=(R;\varphi_0)$ and $I_R^{\mathrm{dw}}=(R;\varphi_0)$, respectively.

After that, we transform the range images $I_R^{\mathrm{up}}=(R;\varphi_0)$ and $I_R^{\mathrm{dw}}=(R;\varphi_0)$ from the polar coordinates $(R;\varphi_0)$ to the Cartesian coordinates (x,y), as is shown in Fig. 2, according to

$$\begin{cases} x=R\ \sin(\varphi_0) \\ y=R\ \cos(\varphi_0) \end{cases}, \tag{23}$$

to obtain $I_{xy}^{\mathrm{up}}(x;y;\varphi_0)$ and $I_{xy}^{\mathrm{dw}}(x;y;\varphi_0)$, respectively.

Finally, the radar images that correspond to different azimuth angles φ_0 are spliced together to obtain the 2-D sea surface images $\tilde{I}_{xy}^{\mathrm{up}}(x,y)$ and $\tilde{I}_{xy}^{\mathrm{dw}}(x,y)$ that correspond to the upward LFM signal and downward LFM signal, respectively, which can be expressed by

$$\tilde{I}_{xy}^{\mathrm{up}}(x,y)=\sum_{\varphi_0} I_{xy}^{\mathrm{up}}(x,y;\varphi_0), \tag{24}$$

$$\tilde{I}_{xy}^{\mathrm{dw}}(x,y)=\sum_{\varphi_0} I_{xy}^{\mathrm{dw}}(x,y;\varphi_0). \tag{25}$$

Through the above steps, we can obtain the sea-surface image. In the following section, we will follow the above steps to measure the sea-surface current velocity and provide some basic results.

4 Simulation results

This section presents the radar parameter settings, briefly introduces the simulation results, compares the sea-surface current velocity inversion error between two different signal transmission modes, and displays the imaging results.

4.1 *Ocean scene modeling*

According to the parameter settings of Liu et al. (2017) and Parsa (2014), we set the parameters of the X-band radar combining with the needs of current measurement and imaging. The proposed shore-based radar parameter settings are shown in Table 1.

To begin with, we used the Cartesian coordinate system, as is shown in Fig. 2. According to Raney and Vachon (1988), the height of the sea surface $z_1(x_m,y_n)$ at the spatial coordinates (x_m,y_n) is

$$z_1(x_m,y_n)=\iint \sqrt{p_{\mathrm{w}}(k_x,k_y)}\cos\left(k_x x_m+k_y y_n+\varphi_{k_x,k_y}\right)\mathrm{d}k_x\mathrm{d}k_y, \tag{26}$$

where $p_{\mathrm{w}}(k_x,k_y)$ is the wave energy spectrum. We used the JONSWAP spectrum (Brüning et al., 1990) here. In addition, φ_{k_x,k_y} takes a uniform discrete value in the interval 0–2π and k_x, k_y represent the azimuth wave number and the range wave number, respectively. The sea surface significant wave height was set to 0.2 m for the sea surface simulation. Figure 7 shows the sea-surface height field after the simulation. The stripes on the sea surface can be clearly seen in the figure.

Based on the sea-surface height field that is simulated in the previous step, the effects of long-wave orbital velocity and tilt modulation on the ocean were added. We use uniform current speed and the sea surface height according to the theoretical formula (Luo, 2018) to calculate the normalized radar cross-section (NRCS). Figure 8 shows its NRCS under HH polarization.

The radar's illuminated area is considered to be fan-shaped.

Table 1. Simulation parameters for raw data of the proposed radar

Parameter	Value
Radar platform altitude/m	30
Band width/MHz	30
SNR/dB	56
f_0/GHz	10
Offshore distance/km	5
Pulse duration/ms	1
Radar incidence angle/(°)	85
Main wave wavelength/m	100
Significant wave height/m	0.2
Resolution	5 m× 5 m

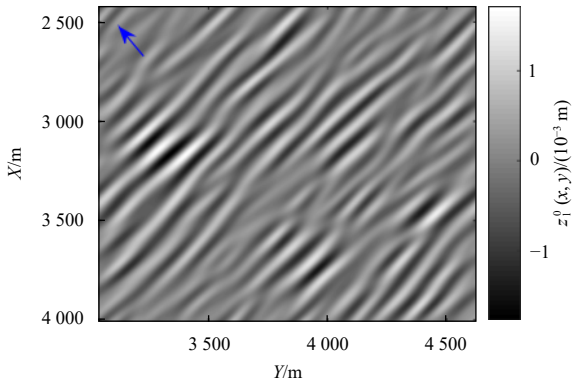

Fig. 7. Sea-surface height. Arrow indicates the direction of wave propagation.

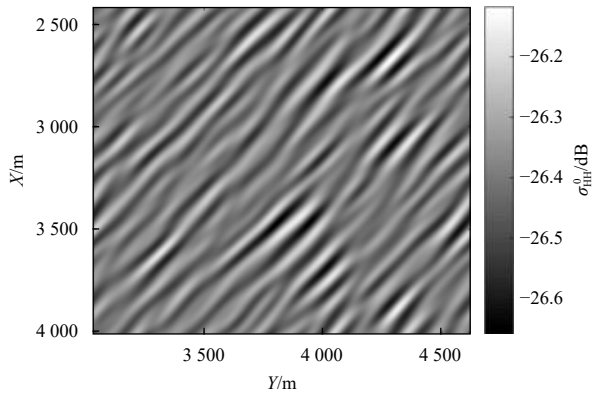

Fig. 8. Normalized backscattering cross-section (NRCS) under HH polarization.

For convenience, we set the polar coordinates to center on the radar. The shaded part in Fig. 2 represents the radar's electromagnetic wave illumination area. We then divided the radar's illumination area into several individual bins and set the number of bins in the radial direction to M and the number of bins in the angular direction to N. Given that simulation of the received echo is required to input the parameters (the sea surface backscattering section, sea-surface height, and orbital velocity) which are generated in the previous step, it is necessary to extract the corresponding parameters from the grid points in the illuminated area. That needs us to transform the data from the polar coordinate system (R_M, φ_N) to the Cartesian coordinate system (x_M, y_N).

The next step is to transform the sea surface backscattering section, sea-surface height, and orbital velocity data from the polar coordinate system (R_M, φ_N) to the Cartesian coordinate system (x_M, y_N) according to the following:

$$\begin{cases} x_M = (R_0 + \Delta R)\sin(\varphi_0 + \Delta\varphi) \\ y_N = (R_0 + \Delta R)\cos(\varphi_0 + \Delta\varphi) \end{cases}, \tag{27}$$

where φ_0 is the radar azimuth, and R_0 is the horizontal distance of the radar platform from the observation area, ΔR represents the distance of a scattering point from the center point, and $\Delta\varphi$ represents the azimuth of this scattering point off the center point. Finally, we find the point closest to (x_M, y_N) in the initially generated current field and extract the parameters (sea-surface height, backscattering section, orbital velocity, and unit impulse response) of the radar system.

The received signal $S_{\text{recv}}(t)$ in the simulation can be expressed as

$$\begin{aligned} S_{\text{recv}}(t) = \sum_{\Delta R}\sum_{\Delta\varphi}\gamma(\Delta R, \Delta\varphi)\left\{W_{\text{r}}\left(t - \frac{2r(t;\Theta)}{c}\right)\mathrm{e}^{\mathrm{j}\pi k_{\text{r}}\left(t-\frac{2r(t;\Theta)}{c}\right)^2} + \right. \\ \left. W_{\text{r}}\left(t - \Delta t - \frac{2r(t;\Theta)}{c}\right)\cdot\mathrm{e}^{-\mathrm{j}\pi k_{\text{r}}\left(t-\Delta t-\frac{2r(t;\Theta)}{c}\right)^2}\right\}\times \\ \mathrm{e}^{\mathrm{j}2\pi f_0\left(t-\frac{2r(t;\Theta)}{c}\right)} + E_n(t), \end{aligned} \tag{28}$$

where $E_n(t)$ is the receiver's thermal noise. Θ, $r(t;\Theta)$ and $\gamma(\Delta R, \Delta\varphi)$ are respectively expressed as

$$\Theta = \left\{R_0, \varphi_0, \Delta R, \Delta\varphi, v_x, v_y, v_{\text{r}}^{\text{wav}}, h\right\}, \tag{29}$$

$$r(t;\Theta) = \sqrt{\left[(R_0 + \Delta R)\ \sin(\varphi_0 + \Delta\varphi) + v_x t\right]^2 + \left[(R_0 + \Delta R)\ \cos(\varphi_0 + \Delta\varphi) + v_y t\right] + h^2} + v_{\text{r}}^{\text{wav}}\cdot t, \tag{30}$$

$$\gamma(\Delta R, \Delta\varphi) = \aleph_{R\varphi}, \tag{31}$$

where v_x, v_y are the component of the current velocity; $v_{\text{r}}^{\text{wav}}$ is the radial long-wave orbital velocity; h is the height of the radar platform; and $\aleph_{R\varphi}$ is a complex circular Gaussian random number, with its expectation set to be zero and its variance set to be NRCS simulated in the previous step $\sigma^0_{\text{HH}}(\Delta R, \Delta\varphi)$, as shown in Eq. (32).

$$E\left\{|\aleph_{R\varphi}|^2\right\} = \sigma^0_{\text{HH}}(\Delta R, \Delta\varphi), \tag{32}$$

where $E\{\cdot\}$ denotes the expectration operator.

4.2 *Velocity measurement*

We use the time-shifted up-and-down CWLFM signals to measure the current velocity in a region. Then, we down-convert the received signal $S_{\text{recv}}(t)$ and separate the upward and downward CWLFM signals. After that, we calculate the phase difference between the upward LFM one-dimensional range image $I_f^{\text{up}}(f)$ and downward LFM one-dimensional range image $I_f^{\text{dw}}(f)$. Because $I_f^{\text{up}}(f)$ and $I_f^{\text{dw}}(f)$ are expressed in the frequency domain, we use t to denote a transform domain of f, to calculate the phase difference between $I_f^{\text{up}}(f)$ and $I_f^{\text{dw}}(f)$ in transform domain. The time in Fig. 9 has no real physical meaning. Figure 9a shows the obtained phase difference. It can be seen from the figure that the phase difference has clutter. Hence, we used the median filter to smooth the phase difference, as shown in Fig. 9b. The clutter with large fluctuations at both ends is mainly due to the change in the bandwidth of the signal and the influence of instrument noise after the signal take absolute value and FT.

We performed a least-squares fit on the phase difference in the interval $-T_{\text{r}} \leqslant t \leqslant T_{\text{r}}$ to fit a straight line. Figure 10 shows the effect after fitting. The red dashed line represents the fitted straight line, and the blue line represents the phase difference. Because the phase difference is proportional to the target velocity, we can calculate the target velocity based on the slope of the fitted straight line.

It can be seen from Fig. 10 that, when we use time-shifted up-and-down CWLFM signals, they exhibit a significant correlation over time. However, Fig. 11 shows the phase difference of simul-

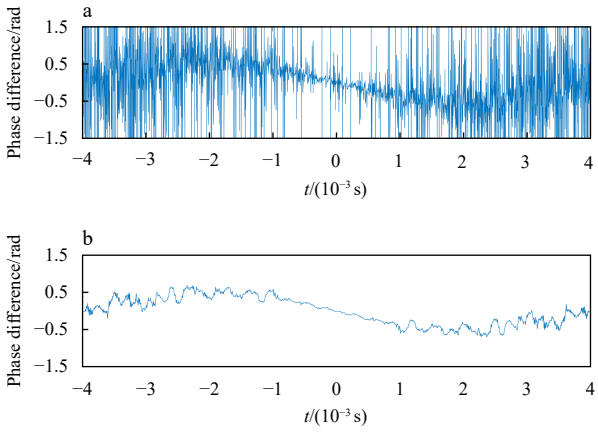

Fig. 9. The phase difference before smoothing (a), and moothed phase difference (b).

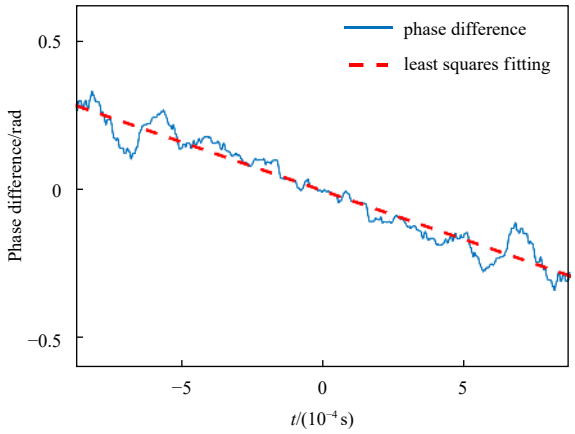

Fig. 10. The phase difference after fitting. The blue solid line is the smoothed phase difference, and the red dashed line is the result of least-squares fitting of the intermediate effective signal.

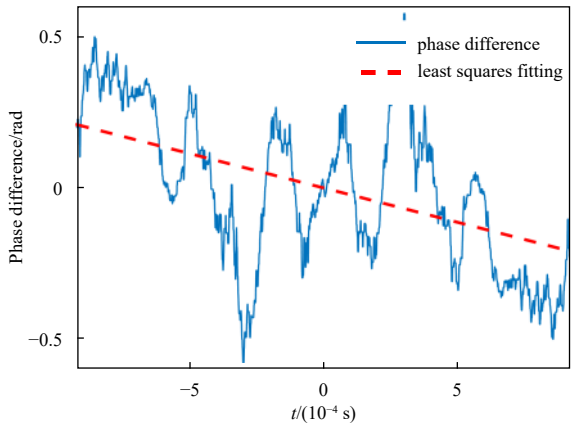

Fig. 11. The phase difference after the least-squares fitting.

taneously transmitted up-and-down LFM signals with the other parameters unchanged. It can be seen from Fig. 11 that the phase difference has no obvious linear relationship with time. After the least-squares fitting, the error is larger. It shows the proposed time-shifted up-and-down method can not only measure the current velocity in a region but also has a better effect than the simultaneously transmitted up-and-down LFM signals.

Table 2 shows the error in the velocity measurement that is obtained by transmitting the time-shifted up-and-down CWLFM signals and simultaneously transmitting the up-and-down LFM signals in 20 Monte Carlo experiments with a measurement area of 10 km. The second column contains the root mean square errors of the velocity measurement using simultaneously transmitted up-and-down LFM signals. The third column contains the root mean square errors of the velocity measurements with time-shifted up-and-down CWLFM signals. By comparing the two columns, it can be seen that, when using the time-shifted up-and-down CWLFM signals to measure the velocity, the error is significantly smaller.

4.3 *Sea-surface imaging*

In addition to the above-mentioned velocity measurement function, the new proposed radar can also perform sea-surface imaging. When we simulated to measure current speed, considering the accuracy of current measurement, we set the offshore distance as 5 km, to reduce the influence of coastal clutter. The parameter we set for imaging is shown in Table 3.

Table 2. Errors in the speed measurement

Real velocity/ (cm·s^{-1})	Simultaneous STD/(cm·s^{-1})	Time-shifted STD/(cm·s^{-1})
0	3.27	2.35
28.18	4.17	1.96
56.35	8.80	2.31
84.53	10.20	2.81

Note: The real velocity column contains the actual radial velocity calculated from the actual input *x*-axis and *y*-axis.

Table 3. Simulation parameters used for imaging

Parameter	Value
Radar platform altitude/m	30
Band width/MHz	30
SNR/dB	56
f_0/GHz	10
Offshore distance/km	1
Resolution	5 m × 5 m

Figure 12a shows a 2-D sea-surface image obtained by splicing all of the 1-D range images when transmitting the time-shifted up-and-down CWLFM signals. Figure 12b shows an image of the sea-surface NRCS obtained by simulation. A comparison of the two figures shows that the radar we designed can achieve sea-surface imaging and distinguish the wavy stripes on the sea surface more clearly.

Figure 13 shows 2-D sea-surface image when simultaneously transmitting the up-and-down LFM signals. We can see from Fig. 13 that the imaging is very blurry, we cannot see the wavy stripes on the sea surface clearly. Comparing Figs 12 and 13, we can find that our radar can image clearly.

5 Conclusions

In this study, we explain the principle of Fois et al.'s (2015) method for current measurement using up-and-down LFM signals in detail. In the process, we found that, when using a shore-based radar to measure the current velocity of a region, the up-and-down LFM signals interfere with each other. Therefore, we proposed a new method for current measurement that uses time-shifted up-and-down CWLFM signals. The proposed signal transmission method solves the problem of interference between upward and downward LFM signals. We also proposed a multifunction radar that transmits the time-shifted up-and-down LFM signals and can not only measure sea-surface currents but can also perform sea-surface imaging. Then, we constructed an algorithm that allows for fast retrieval of the sea-surface current velocity.

However, there remain some shortcomings with our proposed method. For example, we do not concern the effect of rain on the radar performance (Chen et al., 2020; Huang et al., 2017b). We do not derive the theoretical formula, and calculate the theoretical value. In addition, we have only conducted theoretical verification at present, and have not measured data for comparison. In the next step, we plan to derive the theoretical formula and separate surface waves' orbital velocities. In addition, we should consider applying the time-shifted up-and-down CWLFM signals to actual radars, and then using the measured data to prove the feasibility of the principle. In addition, we need to consider the effect of other factors on the radar performance, such as rain, wind.

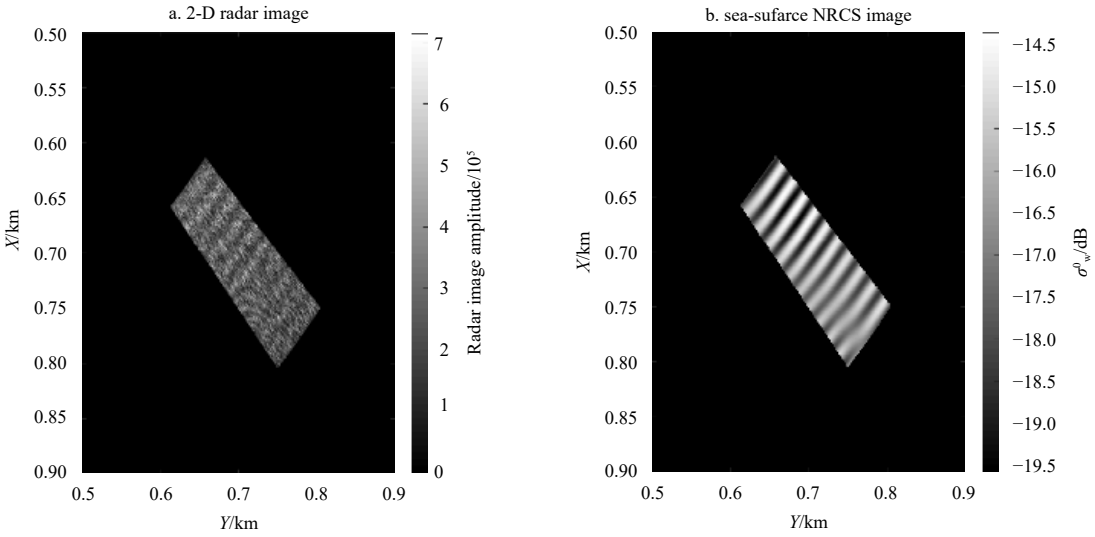

Fig. 12. 2-D radar imaging (a), and sea-surface NRCS imaging (b).

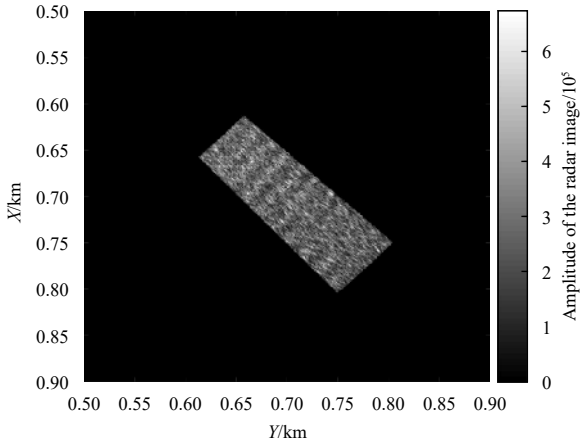

Fig. 13. Radar image by simultaneously transmitting the up-and-down LFM signals.

References

Al-Habashneh A A, Moloney C, Gill E W, et al. 2018. The effect of radar ocean surface sampling on wave spectrum estimation using X-band marine radar. IEEE Access, 6: 17570–17585, doi: 10.1109/ACCESS.2018.2821564

Bao Qingliu, Dong Xiaolong, Zhu Di, et al. 2015. The feasibility of ocean surface current measurement using pencil-beam rotating scatterometer. IEEE Journal of Selected Topics in Applied Earth Observations and Remote Sensing, 8(7): 3441–3451, doi: 10.1109/JSTARS.2015.2414451

Barrick D. 1972. First-order theory and analysis of MF/HF/VHF scatter from the sea. IEEE Transactions on Antennas and Propagation, 20(1): 2–10, doi: 10.1109/TAP.1972.1140123

Brüning C, Alpers W, Hasselmann K. 1990. Monte-Carlo simulation studies of the nonlinear imaging of a two dimensional surface wave field by a synthetic aperture radar. International Journal of Remote Sensing, 11(10): 1695–1727, doi: 10.1080/01431169008955125

Carrasco R, Horstmann J, Seemann J. 2017. Significant wave height measured by coherent X-band radar. IEEE Transactions on Geoscience and Remote Sensing, 55(9): 5355–5365, doi: 10.1109/TGRS.2017.2706067

Chen Xinwei, Huang Weimin, Zhao Chen. 2020. Rain detection from X-band marine radar images: A support vector machine-based approach. IEEE Transactions on Geoscience and Remote Sensing, 58(3): 2115–2123, doi: 10.1109/TGRS.2019.2953143

Fois F, Hoogeboom P, Chevalier F L, et al. 2015. DopSCAT: A mission concept for simultaneous measurements of marine winds and surface currents. Journal of Geophysical Research: Oceans, 120(12): 7857–7879, doi: 10.1002/2015JC011011

Gangeskar R. 2018. Verifying high-accuracy ocean surface current measurements by X-band radar for fixed and moving installations. IEEE Transactions on Geoscience and Remote Sensing, 56(8): 4845–4855, doi: 10.1109/TGRS.2018.2840133

Huang Weimin, Liu Xinlong, Gill E W. 2017a. An empirical mode decomposition method for sea surface wind measurements from X-band nautical radar data. IEEE Transactions on Geoscience and Remote Sensing, 55(11): 6218–6227, doi: 10.1109/TGRS.2017.2723431

Huang Weimin, Liu Xinlong, Gill E W. 2017b. Ocean wind and wave measurements using X-band marine radar: A comprehensive review. Remote Sensing, 9(12): 1261, doi: 10.3390/rs9121261

Klemas V. 2012. Remote sensing of coastal and ocean currents: an overview. Journal of Coastal Research, 28(3): 576–586, doi: 10.2112/JCOASTRES-D-11-00197.1

Liu Xinlong, Huang Weimin, Gill E W. 2017. Estimation of significant wave height from X-band marine radar images based on ensemble empirical mode decomposition. IEEE Geoscience and Remote Sensing Letters, 14(10): 1740–1744, doi: 10.1109/LGRS.2017.2733538

Lund B, Graber H C, Romeiser R. 2012. Wind retrieval from shipborne nautical X-band radar data. IEEE Transactions on Geoscience and Remote Sensing, 50(10): 3800–3811, doi: 10.1109/TGRS.2012.2186457

Luo Gen. 2018. Electromagnetic scattering from sea surface with dihedral corner model of breaking wave at large incident angles. Journal of Jiangxi Science & Technology Normal University (in Chinese), (6): 89–95

Maresca S, Braca P, Grasso R, et al. 2014. Multiple oceanographic HF surface-wave radars applied to maritime surveillance. In: Proceedings of the 17th International Conference on Information Fusion. Salamanca, Spain: IEEE

Parsa A. 2014. Fast moving target detection in sea clutter using non-coherent X-band radar. In: Proceedings of 2014 IEEE Radar Conference. Cincinnati, OH, USA: IEEE

Raney R K, Vachon P W. 1988. Synthetic aperture radar imaging of ocean waves from an airborne platform: focus and tracking issues. Journal of Geophysical Research: Oceans, 93(C10): 12475–12486, doi: 10.1029/JC093iC10p12475

Seemann J, Carrasco R, Stresser M, et al. 2017. An operational wave

monitoring system based on a Dopplerized marine radar. In: Proceedings of the OCEANS 2017-Aberdeen. Aberdeen, UK: IEEE

Senet C M, Seemann J, Flampouris S, et al. 2008. Determination of bathymetric and current maps by the method DiSC based on the analysis of nautical X-band radar image sequences of the sea surface (November 2007). IEEE Transactions on Geoscience and Remote Sensing, 46(8): 2267–2279, doi: 10.1109/TGRS.2008.916474

Wang Fuyou, Yuan Gannan, Lu Zhizhong. 2007. Investigation of real-time wave height measurement using X-band navigation radar. In: Proceedings of 2007 International Conference on Wireless Communications, Networking and Mobile Computing. Shanghai, China: IEEE

Wright J. 1968. A new model for sea clutter. IEEE Transactions on Antennas and Propagation, 16(2): 217–223, doi: 10.1109/TAP.1968.1139147

Young I R, Rosenthal W, Ziemer F. 1985. A three-dimensional analysis of marine radar images for the determination of ocean wave directionality and surface currents. Journal of Geophysical Research: Oceans, 90(C1): 1049–1059, doi: 10.1029/JC090iC01p01049

Zhang Jie, Zou Bin, Feng Qian. 2016. An algorithm study of sea current retrieval based on multiple sensor data onboard HY-2 satellite. Marine Forecasts (in Chinese), 33(4): 53–57